REPORT DOCUMENTATION PAGE	*Form Approved* **OMB No. 0704-0188**

1. REPORT DATE *(DD-MM-YYYY)* 13-08-2013	**2. REPORT TYPE** Final	**3. DATES COVERED** *(From - To)* October 2008 - December 2013

4. TITLE AND SUBTITLE Advancement and Application of Multi-Phase CFD Modeling to High Speed Supercavitating Flows	**5a. CONTRACT NUMBER**
	5b. GRANT NUMBER N00014-09-1-0042
	5c. PROGRAM ELEMENT NUMBER
6. AUTHOR(S) Jules W. Lindau and Michael P. Kinzel	**5d. PROJECT NUMBER** 16247
	5e. TASK NUMBER
	5f. WORK UNIT NUMBER
7. PERFORMING ORGANIZATION NAME(S) AND ADDRESS(ES) THE PENNSYLVANIA STATE UNIVERSITY APPLIED RESEARCH LABORATORY OFFICE OF SPONSORED PROGRAMS 110 TECHNOLOGY CENTER BUILDING UNIVERSITY PARK, PA 16802-7000	**8. PERFORMING ORGANIZATION REPORT NUMBER**
9. SPONSORING/MONITORING AGENCY NAME(S) AND ADDRESS(ES) Office of Naval Research 875 North Randolph Street Arlington, VA 22203-1995	**10. SPONSOR/MONITOR'S ACRONYM(S)** ONR
	11. SPONSORING/MONITORING AGENCY REPORT NUMBER

12. DISTRIBUTION AVAILABILITY STATEMENT
Statement A

20130819014

13. SUPPLEMENTARY NOTES

14. ABSTRACT

In this work, we present insight on the internal gaseous flow of artificially ventilated supercavities. Using multiphase computational fluid dynamics, the major mechanism of gas leakage from a ventilated supercavity is identified as occurring though gaseous shear layers forming at the gas-water interface. These observations corroborate previous theory developed for toroidal cavities, and display evidence that shear-layer mechanisms remain important for twin-vortex cavities and cavities interacting with bodies. Additionally, shear mechanisms appear to influence cavity hysteresis behavior. These observations are used to guide improved supercavitating-vehicle analyses including numerical predictions, experiments, and modeling

15. SUBJECT TERMS
supercavitation, computational fluid dynamics, multiphase flow

16. SECURITY CLASSIFICATION OF:			**17. LIMITATION OF ABSTRACT** U	**18. NUMBER OF PAGES** 29	**19a. NAME OF RESPONSIBLE PERSON** Jules W. Lindau
a. REPORT U	**b. ABSTRACT** U	**c. THIS PAGE** U			**19b. TELEPONE NUMBER (*Include area code*)** 814-404-9948

FINAL REPORT: Advancement and Application of Multi-Phase CFD Modeling to High Speed Supercavitating Flows

Michael P. Kinzel **Jules W. Lindau**

Penn State University

Applied Research Laboratory

State College, PA, USA

ABSTRACT

In this work, we present insight on the internal gaseous flow of artificially ventilated supercavities. Using multiphase computational fluid dynamics, the major mechanism of gas leakage from a ventilated supercavity is identified as occurring though gaseous shear layers forming at the gas-water interface. These observations corroborate previous theory developed for toroidal cavities, and display evidence that shear-layer mechanisms remain important for twin-vortex cavities and cavities interacting with bodies. Additionally, shear mechanisms appear to influence cavity hysteresis behavior. These observations are used to guide improved supercavitating-vehicle analyses including numerical predictions, experiments, and modeling.

INTRODUCTION

Supercavitating vehicles are underwater vehicles contained in a gaseous cavity (or supercavity) with the overall goal of drag reduction. This drag reduction is achieved by virtually eliminating the viscous drag components on a vehicle hull. These gaseous cavities can be formed by either ventilating gas or vaporizing the liquid. Ventilated cavities are the most favorable type for practical purposes, as such cavities are controllable. The cavity can then be stabilized, thus, mitigating buffeting, surface damage, large-scale vehicle vibrations, and other negative consequences typical to cavitation. Supercavitation is one, of many, practical underwater-vehicle concepts with potential to significantly increase underwater vehicle speeds.

Gas entrainment is studied because of its clear impact on supercavitating-vehicle design. In steady operation, the ventilation requirement for a supercavity is equal to the amount of gas being entrained from the cavity. Thus, the gas entrainment rate is directly related to gas storage requirements. The cavity shape can also be approximated using the gas-entrainment rate. These models become useful for designing hull forms, positioning of control surfaces, as well as developing vehicle-controller models. These benefits creates the need for physically-accurate, design-level models that approximate the cavity shape based on a gas-ventilation rate. Such models can only be developed with an understanding of the physical processes that govern them.

In this work, computational fluid dynamics (CFD) simulations are used to improve the understanding of supercavitating flows. The results contain evidence that corroborates the theory of Spurk [1], which ties the gas entrainment to shear layers forming on the cavity interface. Although the original work was limited to toroidal-vortex closing cavities [1], the present CFD solutions contain evidence that the cavity-shear layers remain a primary gas-entrainment mechanism for twin-vortex-closing cavities. These insights reveal improved CFD formulations for supercavitation, help to develop reliable models of the process, and improve the interpretation of scale-model experiments.

BACKGROUND

Theories developed for modeling supercavities, supercavity cavity-closure modes, and the impact that these closure modes have on gas entrainment are reviewed. Note that the reviewed models and investigations are restricted to horizontal supercavities, therefore, buoyancy is assumed to act perpendicular to the free stream velocity.

Classical Models of Supercavities

Scaling Parameters

Several nondimensional parameters are useful to present the behavior of ventilated supercavities. The cavitation number, σ_c, is defined as

$$\sigma_c = 2\frac{p_\infty - p}{\rho_\infty V_\infty^2} \qquad (1)$$

The gas-ventilation rate, Q, can be nondimensionalized by the cavitator diameter, D_N, and the free-stream speed, V_∞ resulting in the gas entrainment coefficient, C_Q,

$$C_Q = \frac{Q}{V_\infty D_N^2} . \qquad (2)$$

Lastly, the Froude number, Fr_N, is a scaling parameter given by

$$Fr_N = \frac{V_\infty}{\sqrt{gD_N}} , \qquad (3)$$

where g is the gravitational acceleration. These are the primary scaling parameters considered in supercavitation. However, in many cases these parameters are rescaled using an *equivalent disk-cavitator diameter*, $D_{N,Disk}$, defined as

$$D_{N,Disk} = D_N\sqrt{\frac{c_D}{c_{D,Disk}}} . \qquad (4)$$

Note that the drag coefficient, c_D, is defined as $D/(\rho_\infty V_\infty^2 D_N^2 \pi/4)$. $D_{N,Disk}$ refers to the size of a flat, circular-disk cavitator that produces the same drag as another cavitator (of any shape). This modified scaling becomes convenient as the cavity shape and ventilation rate scale with cavitator drag [4]. Thus, data from canonical cavitators (such as a disk) can be used to approximate cavity behavior forming over different cavitators. This is accomplished by replacing D_N with $D_{N,Disk}$ within all of the scaling parameters.

Other scaling parameters exist, but are readily considered less significant. Viscous effects are secondary, thus, Reynolds number ($Re_N = \rho_\infty V_\infty D_N \mu_\infty^{-1}$) scaling is rarely considered. Lack of viscous scaling is supported by experiments for the cavitator drag and the cavity shape over a range of Reynolds numbers [2]. However, viscous scaling importance can be inferred from other experiments. Experiments of Epshtein suggest that the microscale gas-entrainment processes are altered over different Re_N values [6]. Similarly, surface tension (scaled via the Weber number, $We = \rho_\infty V_\infty^2 \sigma^{-1}$) is rarely considered in supercavitation. It was also determined, experimentally, that surface tension also impacts the microscale gas-entrainment processes suggesting importance in scaling We [6].

Cavity Shape Approximations

Semi-empirical approximations of the cavity shape exist by correcting the analytic, potential-flow based, solution with $\sigma_c = 0$ [4]. These methods use geometric (cavitator radius, R_N) and integral parameters (c_D and σ) to define the cavity shape. In this work, the models are based on the those reviewed by Semenenko [3].

Consider cavity-size approximations. The maximum cavity radius, R_c may be approximated using Eq. 5.

$$R_c = R_{N,Disk} \sqrt{\frac{c_{D,Disk}}{k\sigma}} \qquad (5)$$

The parameter k, in Eq. 5, remains near 1.0 [3]. An approximate cavity length, L_c, can be computed as

$$L_c = 2R_{N,Disk} A \frac{\sqrt{c_{D,Disk}}}{\sigma} = 2R_c A\sqrt{k}\,. \qquad (6)$$

Another parameter, A, takes values near 2.0. Finally, the axial profile, $R(x)$, can be expressed as a function of cavity length as

$$R(x) = \begin{cases} R_N\left(1+3x/R_N\right)^{1/3} & for: x \le x_1 \\ R_c\sqrt{1-\left(1-\frac{R_1^2}{R_c^2}\right)\left[1-2\left(x-x_1\right)\left(L_c-2x_1\right)^{-1}\right]^{2/\kappa}} & for: x > x_1 \end{cases} \qquad (7)$$

In this relation, the κ parameter is introduced and remains near 1.0. Also, x_1 is the location where two profile relations are matched. A cavitator-dependent approximation for $x \le x_1$ is intended to capture the cavity profile from the separation point on the cavitator to x_1. The one-third power relation, for $x \le x_1$, is suited to approximate cavities detaching from disk-shaped cavitators. However, for other cavitator shapes this relation may be replaced. For $x > x_1$, the relation is a semi-analytic cavity shape. The second relation is initialized to match the first relation at an x_1 of $2R_N$.

Finally, the vertical displacement of a cavity, *h(x)*, can be determined using momentum theorem. Vertical cavity deflections arise from forces both cavity buoyancy and downwash from lifting cavitators. These effects can be computed using relations from Logvinovich [4], as

$$h(x)=\left[\frac{|g|}{\pi V_\infty^2}\int_0^x \frac{V_I(s)}{R(s)^2}ds\right]_{bouyancy}-\left[\frac{c_L D_N^2}{4}\int_0^x \frac{1}{R(s)^2}ds\right]_{Lift}. \tag{8}$$

Here, $R(s)$ is the local cavity radius and $V_I(s)$ is the integrated volume of the cavity gas occupied from $x=0$ to s. Note that the separate gravity- and lift-induced terms are indicated with subscripts. The cavitator-lift coefficient, c_L, is defined as $L/(\rho_\infty V_\infty^2 D_N^2 \pi/4)$.

When properly applied, the preceding relations provide an efficient, and accurate, prediction method of cavity shapes. For isolated supercavities, the only unknown quantities are the cavitator forces, i.e. c_L and c_D. V_∞ ρ_∞, and σ_c are specified. k, κ, and A must be determined from experience. Note that we apply the values reported in the summary of Semeneko [3]. As the ventilation rate for the specified σ_c remains unknown, a closure is needed. This is achieved by relating gas-entrainment rate to a given cavity pressure, σ_c. Need for this relation motivates the present work.

Cavity-Closure Modes

The cavity-closure pattern significantly impacts gas entrainment rate. In this work, two closure patterns are considered: (1) twin-vortex and (2) toroidal-vortex closures. Diagrams of the cavity types are displayed in the right portion of Fig. **1**.

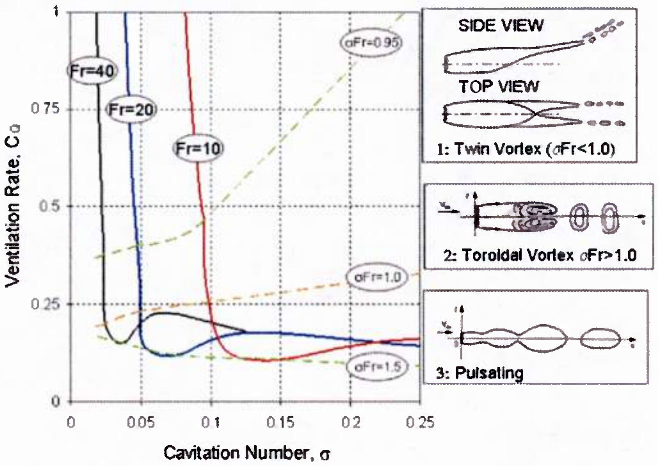

Figure 1: Sample C_Q-σ curve with corresponding cavity types. The diagrams displaying the cavity shapes are from Semenenko [3].

Twin-vortex closing cavities are longer and appear more stable. With an increased length the cavities experience stronger buoyant effects. As depicted in the diagram in Fig. **1**, these cavities are characterized by a pair of axially aligned vortices forming at the cavity-closure location. These twin vortices instantaneously contain all (or nearly all) the gas entrained from the cavity. The formation of either a twin vortex or toroidal cavity has been shown, via empirical evidence [5], to be dependent on the $\sigma Fr_{N,Disk}$ value. When values are less than one, the twin-vortex closure appears. For values greater than one, toriodal closure is expected.

A toroidal cavity forms behind the same cavitator and at the same velocity, but at lower ventilation rates. Toroidal-vortex cavities are relatively small, unsteady, cavities with little-to-no gravitational effects. As displayed in the diagram in Fig. **1**, these cavities close with axisymmetric, reentrant jets that evolve into toroid-shaped vortices that shed from the cavity. These gas-filled vortices continually shed pockets gas from the cavity, creating an unsteady shedding process. Such a process could induce undesirable, unsteady loading on vehicle components.

Gas-Entrainment Models

Physically-based models for C_Q as a function of the cavity size have been developed throughout the literature. Because of the cavity size dependence on σ_c (recall Eqs. 5 and 6.), these models are described in terms of σ_c (i.e. $C_Q(\sigma_c)$ models). Sample plots of $C_Q(\sigma_c)$ are given in Fig. **1**. Several important points can be drawn from these plots. These curves are greatly spaced indicating a clear Froude-number dependency. Along each Froude number curve, there is a discontinuity that distinguishes the twin-vortex and toriodal cavities. As indicated in the figure, the left-most portion of the curves are regions where twin-vortex cavities form. The right-most portions are where toriodal cavities form. In general, the cavitation number is asymptotically less sensitive to the ventilation rate for twin-vortex than for toroidal cavities. At each Froude number, there is a region where the cavitation number, as a function of C_Q, is non-unique, implying a region of hysteresis. Correctly capturing these features present a challenge to model development.

Gas Entrainment from Twin-Vortex Cavities

Models for gas-entrainment from twin-vortex cavities are based on modeling the amount of air exiting through the vortex tubes. Campbell and Hilborne [5] presented a frequently applied model based on a correlation of the circulation to the buoyant loads acting on the cavity. The circulation about the cavity centerline can then be conserved about the twin-vortex tubes enabling an estimation of the twin-vortex-core area. Multiplying this area by an approximation of the mean axial velocity through the tube yields a gas entrainment rate (Eq. 9). Note that V_{VT} is the velocity of gas exiting the vortex tubes. Using approximations of R_C and L_C that are similar (but different) to those in Eqs. 5 and 6, and assuming that V_{VT} is V_∞ Eq. 9 becomes the Campbell and Hilborne [5] gas entrainment model, which is provided in the right-most relation in Eq. 9.

$$C_{Q,CH} = \frac{\pi}{32 Fr_{N,Disk}^4 \sigma_c}\left(\frac{V_{VT}}{V_\infty}\right)\left(\frac{D_C}{D_{N,Disk}}\frac{L_C}{D_{N,Disk}}\right)^2 \approx \frac{\pi}{15.8 Fr_{N,Disk}^4 \sigma_c^4} \qquad (9)$$

Note that Campbell and Hilborne [5] speculate that differences between experiment and theory result from errors in assuming that $V_{VT}=V_\infty$ For future uses, a modified Campbell and Hilborne [5] model is considered. Eq. 9 can be rewritten such that improved models of V_{VT} may be considered and using modified approximations for $D_C/D_{N,Disk}$ and $L_C/D_{N,Disk}$, i.e. those given in Eqs. 5 and 6, respectively. This modified form is presented as

$$C_{Q,CHm} \approx \frac{\pi A^2 (1+\sigma_c)^2}{47.6 k Fr_{N,Disk}^4 \sigma_c^4}\left(\frac{V_{VT}}{V_\infty}\right). \qquad (10)$$

Note that within this expression a disk-drag behavior from May [2], $c_{D,Disk} \approx 0.82(1+\sigma)$, is assumed.

Gas Entrainment from Toroidal-Vortex Cavities

The gas entrainment from cavities closing in a toroidal-vortex pattern occurs via gaseous, toroidal-shaped, shedding cavities. Using high-speed photography, Epshtein [6] demonstrated that the entrained gas is a result of a reentrant jet splashing on the cavity walls, creating microcavities that eventually exit the cavity through these toroidal-vortical structures. These microcavities, and the resultant gas entrainment rate, were shown to be influenced by both viscous and surface-tension effects [6]. More recent theory of Spurk [1] suggests that the gas existing the cavity is transported though interfacial shear layers. This shear-layer gas consists of the gas filling the microcavities and subsequent toroidal cavities. Spurk's concept [1] is presented in Fig. 2, the figure illustrates a developed cavity-gas shear layer. The concept is further verified in the expcrimental data of Epshtein [6] that exhibits strong Reynolds number effects in the toroidal-vortex regime. We note that the concept of cavity-shear layers dragging gas from the cavity was previously hypothesized, as mentioned in May [2]. However, it was only recently incorporated into a useful, validated, gas entrainment model [1].

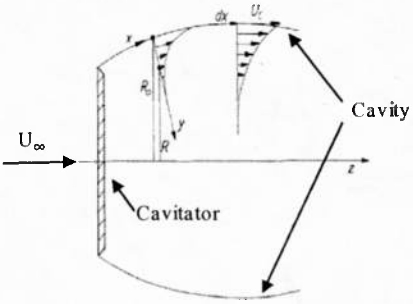

Figure 2: Diagram of the gas-boundary layers within a cavity, theorized as an important mechanism for gas entrainment. The diagram is from Spurk [1].

The results presented by Spurk [1] agree well with experimental measurements at high Fr_N conditions and for reentrant cavities with little buoyant effects. In a reduced form, Spurk's gas-entrainment model is given as

$$C_{Q,Spurk} = k_Q \frac{(1+\sigma_c)}{\sigma_c}\sqrt{\frac{1}{\sigma_c}\ln\frac{1}{\sigma_c}}, \qquad (11)$$

where k_Q is an empirically factor that may be calibrated using a single reentrant-cavity data point. Note that alternate forms of this entrainment model are based on laminar or turbulent shear layers [1]. However, this semi-empirical form can be tuned to handle both laminar, turbulent, or transitional shear layers. Also, scaling the effects of microcavities (*We* and *Re*-dependent features) could also be captured using Eq. 11 as k_Q automatically accounts for the gas within these microcavities.

DESCRIPTION OF COMPUTATIONAL METHODS

The computations used in these studies use multiphase CFD. The CFD method is based on the finite-volume method that solves a form of the Navier-Stokes equations in both the gaseous and liquid regions. These simulations use higher-order numerics, RANS/DES/MILES turbulence modeling, and structured-overset grids. Additional details of the solver are described in Lindau *et al.* [7]. Spatial and temporal requirements have already been determined sufficient by Kinzel [8].

COMPUTATIONAL RESULTS

The mechanisms of gas entrainment are examined using CFD simulations of supercavitating-fluid flows. Details of select flow solutions reported in Kinzel [8] are presented here.

Description of Test Cases

Models of isolated cavitators and cavities interacting with bodies are used to cover the expected range of cavity closure types in these studies. Details of the test cases are given below.

Axisymmetric Disk Cavitator

An isolated disk cavitator represents a basic supercavitating flow. The configuration is displayed in Fig. **3** (a). Several conditions are modeled for this geometry. A limiting case with no gravity ($Fr_N=\infty$), $Re_N=90\times10^6$, and $C_Q=0.5$. And cases based on the experiments of Campbell and Hilborne [5] with $Fr_N=15.54$ over Reynolds numbers from $Re_N=6.2\times10^2$ to 6.2×10^6. For the buoyant cases, the solution is three-dimensional with assumed lateral symmetry. Otherwise, axisymmetric meshes are used.

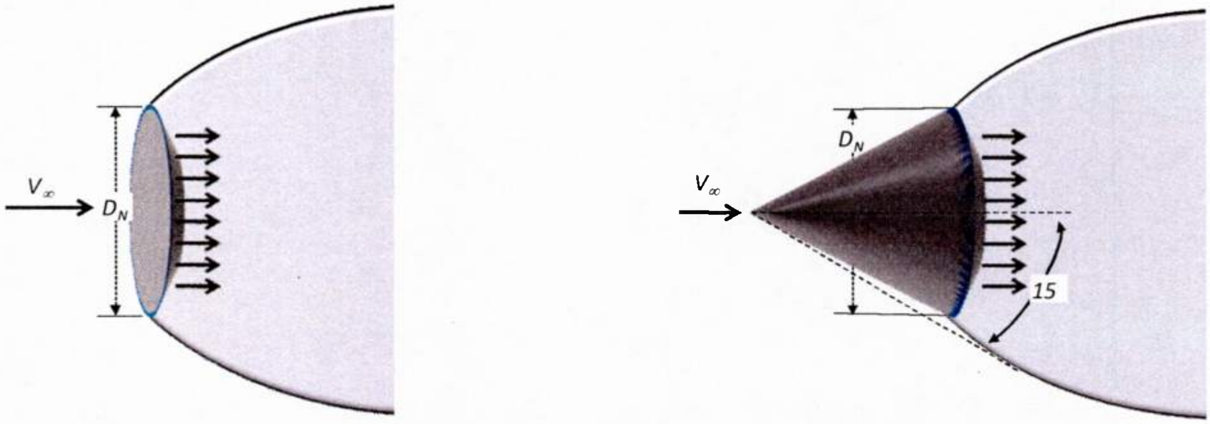

(a) isolated disk cavitator *(b) isolated 15° cone cavitator*

Figure 3: Diagram displaying the isolated cavitator test cases.

Cone-Shaped Cavitator

A 15°-half-angle, conical cavitator (displayed in Fig. **3** (b)) based on a summary of experiments by Kiceniuk [9] is also investigated. The cavitator is set to a lifting configuration that is relevant for trimming or maneuvering a vehicle. The corresponding conditions are: $Re_N=3.2\times10^7$, $Fr_N=72.0$, and $C_Q=1.0$.

Supercavitating Body

Lastly, a case with significant cavity-body interactions is investigated. The case is based on experiments conducted in the University of Minnesota, St. Anthony Falls Laboratory's high-speed water tunnel [10][11]. A diagram representing the test setup is given in Fig **4**. Conditions corresponding to Re_N of 56,000, Fr_N=26.7, and a range of C_Q values were simulated. Results compare favorably with the experiments. However, good results require modeling the support strut, implying a full three-dimensional model is needed [12]. The geometry of the body is modeled as specified by Schauer [11]. However, since it does not impact the physics under consideration, in work reported here the aforementioned support strut is omitted.

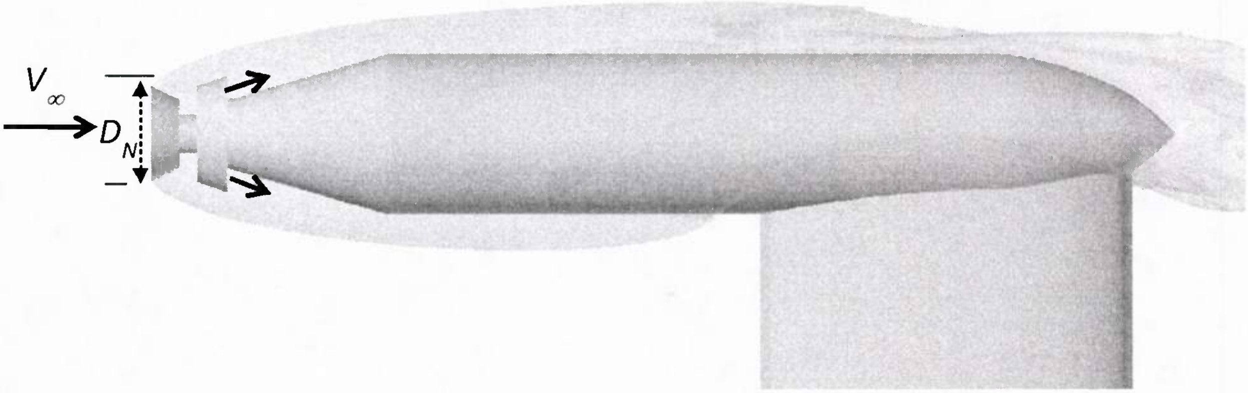

Figure 4: Diagram displaying the cavity-body interaction test case.

Gas Entrainment Behavior

CFD solutions are interrogated to ascertain the dominate mechanisms of air entrainment. In order to highlight regions of axial moving gas, a local rate of gas entrainment is defined as

$$C_{Q,l} = \alpha_g \, u / V_\infty \,. \tag{12}$$

This variable indicates the local, aftward-moving gas through a cavity. Note that its time-averaged surface integral over a given y-z plane aft of the cavitator is equivalent to the overall gas-entrainment rate. This parameter is used to highlight regions of gas entrainment.

Cavity Gas Escaping a Twin-Vortex Cavity

We first investigate the air-entrainment from a twin-vortex cavity. Consider the solution of a twin-vortex supercavity forming behind a cone-shaped cavitator presented in Fig. **5**. In these plots, a grey-scale contour plot along the symmetry plane highlights the cavity region (indicated in black). Note that a pseudo body within in the cavity is colored white. The colored-spectrum contour-line plots, at select axial locations, display the $C_{Q,l}$ profile along the cavity axis.

Consider the $C_{Q,l}$-contour plots in Fig. **5** (a). The plots indicate that $C_{Q,l}$ is highest near the cavity interface. Such a condition implies that the aftward gaseous flow is dominated by physics local to the interface region. The most obvious mechanism being water tugging on the gas (via viscous mechanisms) driving this air entrainment.

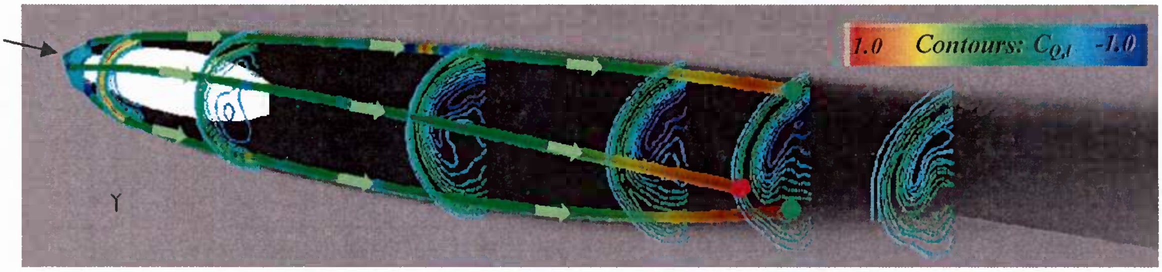

(a) Streamlines traced backwards from the maximum $C_{Q,l}$ regions

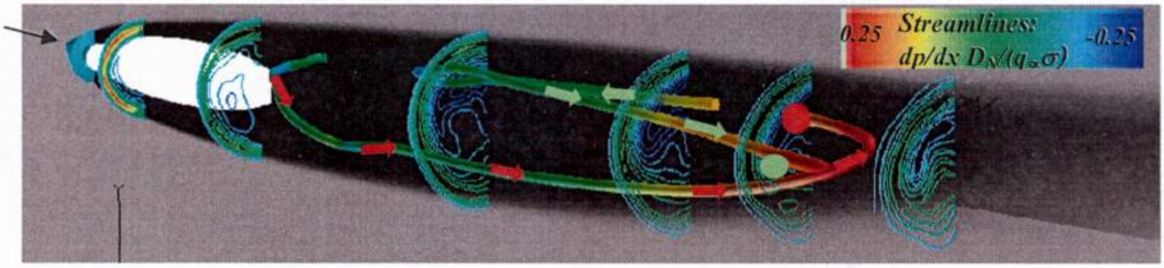

(b) Streamlines traced backwards from the minimum $C_{Q,l}$ regions

Figure 5: Gas flow in a twin vortex cavity formed over a cone-shaped cavitator. The cyan-colored cavitator is moving left-ward with the oncoming velocity indicated (black arrow). The streamlines (colored by pressure gradient and traced backwards in time) indicate the origin of gas entrainment. The colored contour line plots display local gas entrainment rate, $C_{Q,l}$. The grey-shaded contour plot along the centerline is colored by the gas volume fraction (black indicates gas).

In Fig. 5, quasi-steady streamlines are used to demonstrate the *flow history* of gas present in the aft end of the cavity. These streamlines are traced *backwards* in time at various $C_{Q,l}$ magnitudes on the penultimate $C_{Q,l}$-contour plot (originating from the dots). As they originate from such an aft position, it is presumed that positive $C_{Q,l}$ values (green to red) indicate regions where gas will inevitably entrain from the cavity. The negative values highlight regions where gas is recirculating back into the cavity. The history of gas at this position yields insight into gas entrainment.

In Fig. 5 (a), the streamlines indicate entraining gas. There, the streamlines are seeded at the maximum $C_{Q,l}$ levels (at $C_{Q,l}$~0.2), displaying the origin of entraining air. Interestingly, the streamlines originate directly from the injection port. Thus, the injected gas entrains into cavity shear layers and directly out of the cavity.

In Fig. 5 (b), the quasi-steady streamlines highlight recirculating gas. These streamlines are traced from a point the most negative $C_{Q,l}$ values (at $C_{Q,l}$~-0.6), displaying recirculating air. The results display that the gas in the cavity core behaves like a wake. The wake region interacts with the interface shear layer, but the net forward flow in this wake region near zero. In regards to gas entrainment, some gas in the wake region entrains into the interfacial shear layer. This process is similar to that described by Spurk [1]. However, this gas is stripped from the shear layer near the cavity terminus. This "thinning shear layer" region corresponds to an increasing pressure (indicated by the axial-pressure-gradient color on the streamlines). This adverse pressure gradient promotes shear-layer thinning and drives gas recirculation.

Using the results, the picture of the cavity gas flow opposes the conventional thinking that pressure gradients promote the gas to exit the cavity [14]. Recall that most of the reviewed theories completely neglect shear as a mechanism relevant to gas entrainment. Considering these results, it is evident that shear layers play a primary role in gas entrainment. In general, it is obvious that Spurk's hypothesized flow structure dominates gas entrainment from this twin-vortex cavity. However, additional physical processes are apparent. Namely, that these shear layers thin approaching the aft portions of the cavity.

Gas Escaping a Reentrant Cavity Formed Over a Body

Gas entrainment from a partial cavity is now compared to that from a supercavity. In Figs. **6** (a) and (b), streamlines are used to visualize the predicted gaseous cavity flow with the cavity closing on the body (i.e., a partial cavity). In Figs. **6** (c) and (d), these results are contrasted to a modeled supercavity (fully enclosing the vehicle). In **6** (a) and (c), the red streamlines are traced from the cavity interface region. Similar to results shown in Fig. 5, the streamlines indicate a clear path from the ventilation ports, into the shear layers, and out of the cavity. In Figs. **6** (b) and (d), the purple streamlines are seeded within the core of the cavity. In both cases the streamlines indicate that the cavity gas within this region remains nearly isolated and recirculatory. These plots reaffirm the hypothesis of Spurk [1], shear layers remain important with and without cavity-body interactions.

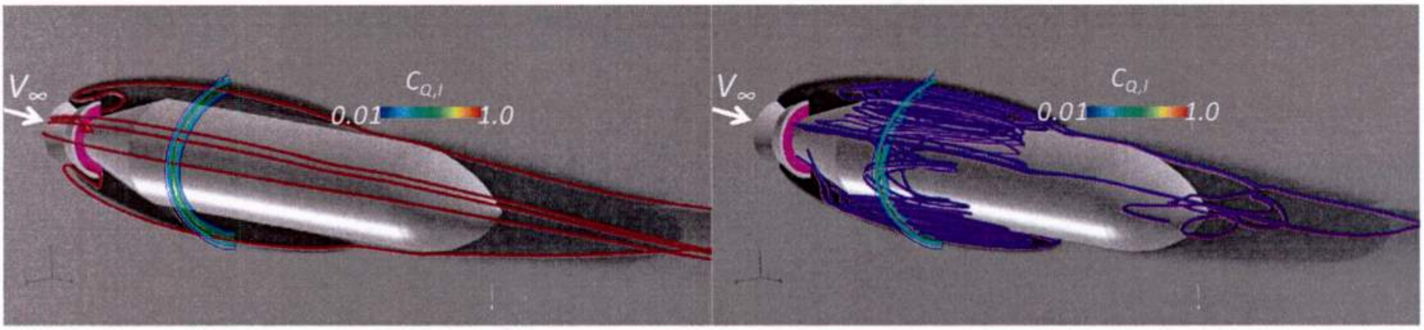

(a) Entrained gas with cavity-body interactions (C_Q=0.45) (b) Recirculated gas with cavity-body interactions (C_Q=0.45)

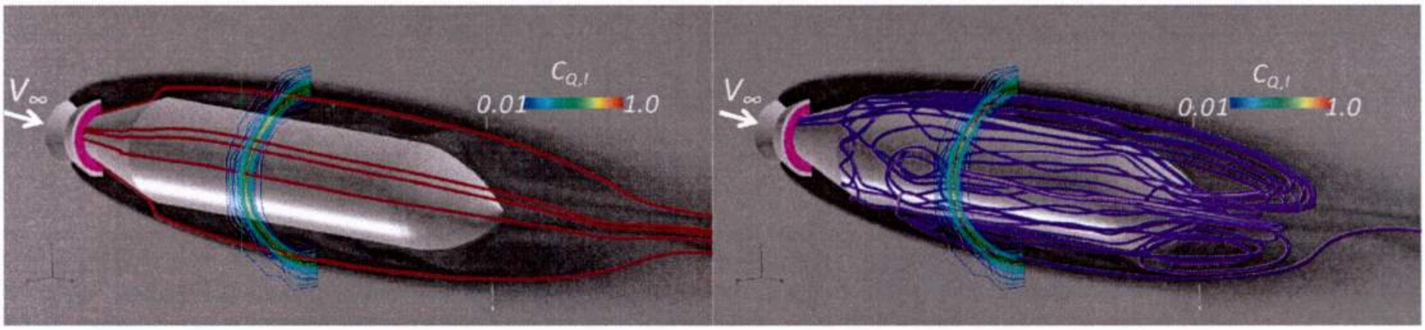

(c) Entrained gas in a supercavity (C_Q=1.0) (d) Recirculated gas in a supercavity (C_Q=1.0)

Figure 6: RANS prediction of the gaseous flow in a ventilated cavity over a body at Fr_N=26.7, Re_N=56,000. Modeled flow for (a-b) a partial cavity (C_Q=0.45) that impacts the body and (c-d) a supercavity (C_Q=0.45). Body is colored gray and inlet ports are colored pink. Colored contour plots indicate $C_{Q.,I}$ at axial location of the maximum cavity-diameter. Streamlines indicate paths of the entrained gas (red) and recirculated gas (purple).

Reynolds Number Effects in a Twin-Vortex Cavity

The reviewed models and simulations suggest that cavity shear layers dominant gas entrainment. Consequently, one would expect that Reynolds number scaling be evident. Results are presented at a range of Reynolds numbers. Most design-level and controller models are based on small-scale experiments. For example, the experiments of Epshtein [6] use a 7 mm diameter cavitator (Re_N=84,000), and Campbell and Hilborne [5] use a 25.4 mm disk cavitator (Re_N=116,000). However, at sea a two to three order-of-magnitude greater Re_N would be expected. In Fig. 7, contour plots of $C_{Q,I}$ are displayed as the Re_N is increased by decades, from 6.2×10^2 to 6.2×10^6. The ventilation port covers about 2/3 of the rear face of the cavitator. The gas jet exiting the port, in particular, appears to be sensitive to Re_N. At increased Re_N (6.2×10^4 to 6.2×10^6) the jet persists axially about two cavitator diameters downstream of the port. Alternatively, for low Re_N values (6.2×10^2 to 6.2×10^3), the jet immediately dissipates and the cavity shear layers thicken just downstream of the separation point from the cavitator. In this vicinity, the shear layer thickening displays a strong Re_N effect. In

Fig. 7, one can easily see the trend of increased shear-layer thickness with a decreasing Re_N. Interestingly, downstream of the dissipated of the jet, the water-attached cavity-shear-layer thickness does not display a strong *Re* effect. However, the wake appears more chaotic. These observations indicate when investigating body-filled cavities that Reynolds-number similarity should be considered.

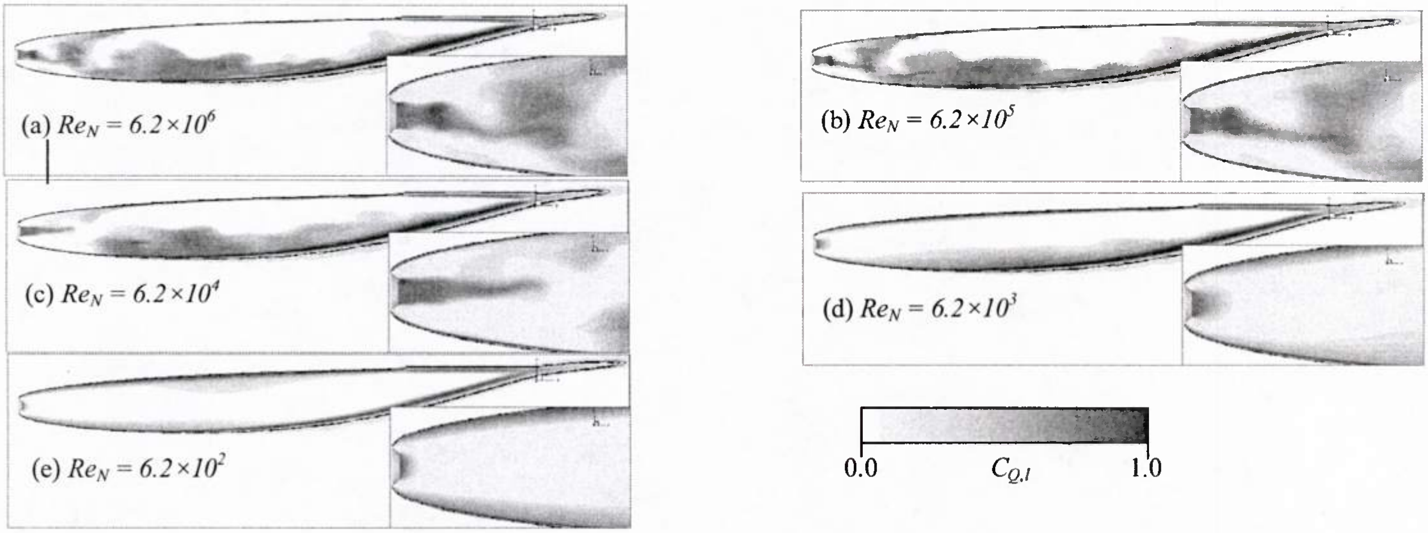

Figure 7: Reynolds number effect on the gas flow in supercavity (C_Q=0.283 and Fr_N=15.54). Filled contour plot through the centerline is $C_{Q,l}$. Cavity interface outlined in black.

DISSCUSSION

The tie between gas-shear layers and the gas entrainment rate impacts numerous aspects of modeling supercavitating flows. In this section, we highlight modeling issues within CFD formulations and discuss needs for improving CFD modeling. Issues with lumped-parameter models are also discussed and improved based on physical observations from the present CFD findings.

CFD Predictions: Sensitivities Arising from Shear-Layer Mechanisms

The predictions of the C_Q-σ_c relation using viscous CFD is sensitive to the models used within these gaseous shear layers [12]. Specifically, predicting C_Q-σ_c has shown to be sensitive to the turbulence modeling approach. In this section, we assess the turbulence model and its impact to modeling shear-layer gas entrainment.

Examination of the Turbulence Model Effects

Turbulence model sensitivities are evaluated for the axisymmetric, disk-cavitator case by comparing results at the extremes of the turbulence model. Thus, cases with and without a RANS-style turbulence model (*RANS* vs. *no TM*) are used to examine this sensitivity. Both cases use an identical computational mesh that has a high-resolution mesh through the interface regions. Specifically, the resolution is $\Delta r \sim 0.01 R_N$, which corresponds to sixty cells through the cavity-interface shear layer.

In Fig. 8, the extracted velocity profiles at an axial location 20.8 radii downstream of the cavitator are compared for the *RANS* and *no TM* results. In this plot, the horizontal axis is a measure of the axial gas velocity and the vertical axis is the distance from the cavity interface. Note that on the horizontal axis, a velocity of one indicates that the gas travels at the same speed and direction as the water. Also, positive velocities indicate forward flow and negative velocities indicate reversed flow. Deviations in the predictions highlight the effect of turbulence in the gaseous shear layer. Examining these deviations, the *No TM* (or laminar) profile displays a thinner shear layer than the *RANS* profile. Thus, the *RANS* model increases the quantity of gas in the shear layer and increases the gas entrainment through shear mechanisms. The direct link between the turbulence model and the quantity of gas within this shear layer implies that the turbulence model has strong potential to affect the C_Q-σ_c relation. A secondary feature, indicated by the roughly constant velocity region just outside of the shear layer, is apparent in the *No TM* profile of Fig. 8. Although not initially obvious, this feature is a result of mass conservation through the steady cavity flow. As identical ventilation rates are prescribed, the integrated gas-mass must be equal between the two cases. Because the *No TM* case displays thinner shear layers, a consistent C_Q is achieved through the increased centerline velocity.

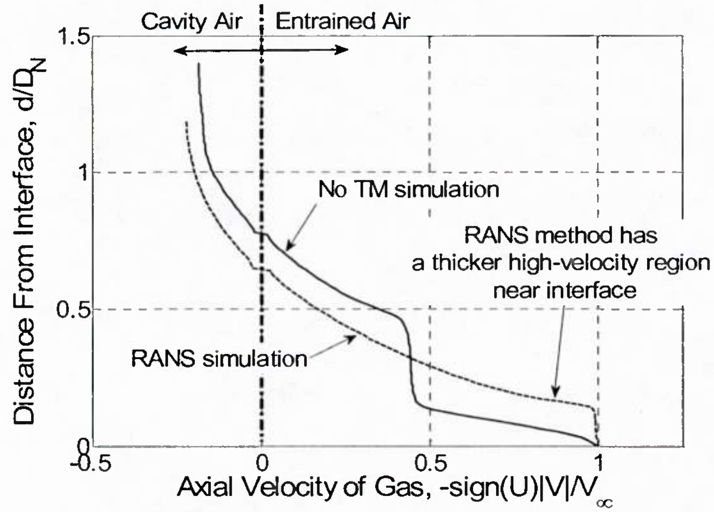

Figure 8: Comparisons in the cavity shear layer velocity profiles between a RANS no turbulence model (no TM) case for an axisymmetric disk cavitator.

Specific Issues with the Turbulence Model Behavior

The turbulence model study is extended to a three-dimensional, unsteady, supercavitating flow with cavity closure on a body. Previous work exhibited that capturing of the correct C_Q-σ_c relation is only feasible for specific turbulence model formulations [12].

Note that this turbulence model sensitivity was only apparent for hysteretic cavities. The results are summarized in Fig. **9** (a). The unsteady RANS (URANS) formulation could not capture the C_Q-σ_c behavior in hysteresis regions. However, with the DES formulation, capturing the C_Q-σ_c relation with hysteresis was recovered. Based on the findings of the previous investigation (exhibiting that turbulence model increases the cavity shear layer, thus increases C_Q value for a given σ_c), the solution sensitivity to the turbulence model formulation can be understood [12].

Consider the perceived improvement using a DES formulation versus URANS. It is customary to model the effect of turbulence on the mean flow via an effective, or eddy, viscosity, ν_t. Thus, the predicted ν_t values are investigated in each case. In DES, a URANS model reverts to large-eddy-simulation-like model for ν_t in regions where the mesh can support eddy structures. This locally diminishes the magnitude of ν_t to values between those of a *RANS* and *No TM* case (recall, from the previous disk-cavitator case). The reduction in modeled turbulence with the DES model, with respect to the URANS model, is verified in Fig. **9**. There, the ν_t, for DES and URANS simulations, are compared for identical conditions. Both cases exhibit a peak in ν_t at the interface, however, the DES simulation exhibits significantly lower ν_t values than the URANS case. As the increased eddy viscosity correlates to increased entrained gas within the shear-layer, the URANS formulation increases the modeled air entrainment rate. These observations imply that the reduced eddy viscosities in the DES model enables the accurate C_Q-σ_c predictions [12], and indicates that a URANS formulation over-estimates the eddy viscosity in these interfacial shear layers.

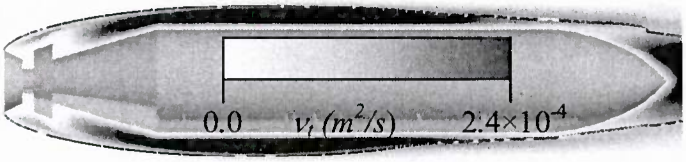

(a) URANS

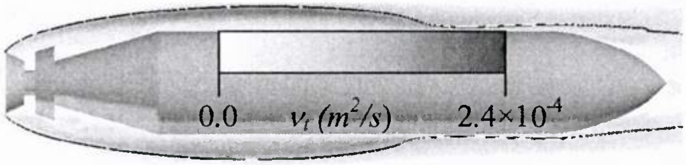

(b) DES

Figure 9: Comparison of URANS and DES predictions.

Consider the cause for this over production of turbulence within the interfacial shear layer. A typical turbulence model is well tuned for wall-bounded flows, but not formulated specifically to an interfacial-shear-layer flow. The turbulence model constants are generally calibrated for each type of shear layer, and further controlled using damping functions to match boundary conditions. As the constants are not tuned and nor is dampening function applied to satisfy a boundary condition at the interface, such an over prediction may be expected. Secondly, these interfacial shear layers are not well understood. The combination of these two issues implies further work to understand these interfacial shears is needed.

In regards to developing an understanding of the interfacial shear layers, we can develop an understanding based on similar problems. Consider that the interfacial shear layer behaves like a boundary layer on a compliant wall. Stability theory for this condition suggests that compliant walls stabilize turbulence, and that when transitioned to turbulence, the turbulence occurs in the form of Kelvin-Helmholtz waves [15]. Thus, in we may expect a significant delay of transition to a turbulent shear layer. Furthermore, when a turbulence model is used, it should be calibrated to a turbulent, Kelvin-Helmholtz-based instability with significant surface tension effects. The properly formulated turbulence model may also apply a dampening function to moderate the turbulence level at the interface. These turbulence model advances are left for future research.

IMPROVED MODELS OF GAS ENTRAINMENT

The present simulations suggest that theory of toriodal cavity-air entrainment [1] is also applicable to buoyant cavities. Using this behavior, we adapt previous gas-entrainment models accordingly. These additions include the observed effects of shear layer contributions to the gas entrainment from a twin-vortex cavity, and the shear-layer gas thinning at the rear of the cavity. Incorporating these observed physical mechanisms into gas entrainment models should provide a more physically accurate model.

Concept Overview

We combine previously developed models, i.e. those of Spurk [1] (based upon cavity-shear layers for toroidal closure cavities) and Campbell and Hilborne [5] (for twin-vortex cavity closure), and include models of a thinning shear-layer to formulate a more physically accurate gas-entrainment model. In Fig. **10**, the model components are depicted within a diagram of a twin-vortex cavity. Estimations of an effective displacement thickness of the shear layer are colored grey. We define a representative velocity within these shear-layer regions, V_{SL}, that correlates to the component of gas entrainment due to shear, i.e. $C_{Q,SL}$. Note that, in general, the shaded-gray regions of the cavity are assumed to travel at the velocity of the neighboring water flow, i.e. $V_{SL} = V_{\infty}\sqrt{1+\sigma}$, however, for simplicity, the velocity of these shear-layer regions, V_{SL}, is assumed to be equal to V_{∞} The regions interior of the shear layers, colored white, is the cavity-flow region. This region has a different representative velocities; here we define one at the maximum cavity diameter, V_C, and another at the twin-vortex core, $V_{VT,p}$. These two velocities correlate to gas entrainment due to pressure-gradient driven effects, $C_{Q,p}$.

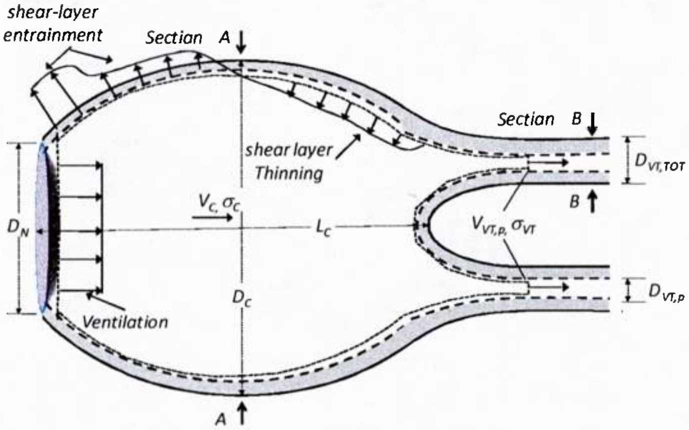

(a) Twin-Vortex Cavity

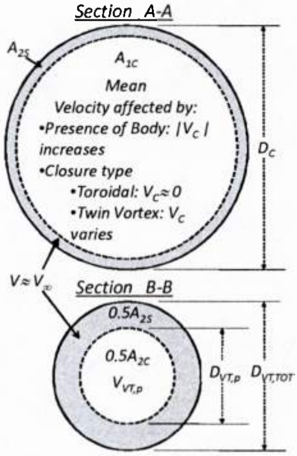

(b) Sectional properties

Figure 10: Elements of economy in a twin-vortex cavity. The gray regions of the cavity represent the gas within the interfacial shear layers. The white regions represent the *cavity* regions, not directly impacted by the water flow. (a) Near-horizontal plane through the cavity containing cavitator, cavity, and both vortex tubes. (b) Two selected axial planes. A-A through the maximum cavity radius location. B-B is through one of the vortex tubes.

Cavity closure type will impact the behavior of the regions described within Fig. **10**. In a toroidal cavity, it can be assumed based on agreement of Spurk's theory with experimental measurements [1], that there is a net-zero axial flow within the *white cavity region*, and that the gray regions comprise of the gas filling the shedding toroidal cavities. This is the only conceivable condition for a toriodal cavity.

Alternatively, a twin-vortex-closing cavity contains two distinct regimes that are distinguished by the limiting case of when $V_c = 0$ and $V_{TV,p} = 0$, which occurs when C_Q=$C_{Q,SL}$. In this special case, the vortex tubes have sufficient cross-sectional area to relieve the gas within the shear layers. The cavity would then behave differently if ventilated higher and lower than this unique value, which are described below:

(1) *Thinning Shear-Layer (TSL) Cavity:* This cavity occurs when $C_Q<C_{Q,SL}$, and implies that $V_c < 0$ and $V_{TV,p} = 0$. In this case, the vortex tubes are too small to support the shear-layer entrained gas. As viscous effects cannot be eliminated, the vortex tubes must be completely filled with $C_{Q,SL}$. This imposes one of two possible conditions: (1) the shear-layer gas accelerates through the vortex tube (i.e. $V_{VT}>V_\infty$), imparting a positive viscous forces component onto the water flow, or (2) the shear-layer gas remains of constant velocity (i.e. $V_{VT}=V_\infty$) through the vortex tubes, and the air is recovered back into the cavity upstream of the tubes. The CFD predictions clearly display that option (2) is favored. Thus, the air in the vortex tube is considered as being $C_{Q,SL}$ minus that recovered via shear-layer thinning. Then, based on a mass balance of the dashed control volume in Fig. **10**, this recovered gas must establish a recirculating cavity behavior.

(2) *Pressure-Driven (PD) Cavity:* When $C_Q>C_{Q,SL}$, an net positive cavity flow forms, $V_c > 0$. This is established when the vortex tubes open to an area larger than the shear-layer gas contains, thus, pressure-gradient driven axial flow can be established through the tubes. This is consistent with the classical theory of Cox and Clayden [14], and would tend to occur for high ventilation rates.

When dividing the gas-entrainment into these two regimes, complex phenomena near the hysteretic cavities can be modeled.

It is worth side tracking for a moment to discuss these effects in regards to application, that is, when a body is present. In the context of the posed cavity regions, if a body is limited to the white-cavity region it will *not interfere with the cavity-shear layer*, thus, it is contended that these entrainment mechanisms remain unaffected. This is consistent with conventional thinking that solid objects internal to an established cavity should not affect the cavity ventilation requirements or shape. However, if the shear-layer regions are altered, the cavity processes can prone to be disturbed; thus, supercavitating hull-forms should consider such effects in their design.

Returning to the air entrainment, the described processes are then used to shape a new model for gas entrainment. The model is composed of two components, given by

$$C_Q = C_{Q,SL} + C_{Q,p}\,. \qquad (13)$$

Here, $C_{Q,SL}$ is the contribution from shear-layer effects, paralleling Spurk [1]. And $C_{Q,p}$ is driven by pressure gradients, relating to the model of Cox and Clayden [14], but is based on the work of Campbell and Hilborne [5].

Shear-Layer Gas Entrainment

First, consider the gas entrained through shear-layer mechanisms. Although the method presented by Spurk [1] fully accounts for the gas entrained into the shear layers, it does not consider the quantity stripped from the shear layer by adverse pressure gradients as observed in the present CFD simulations. This concept is considered as an addition to the model of Spurk.

Recovery Factor

The quantity stripped from the shear-layer, recovered gas, can be determined by considering the remaining mechanisms effecting gas entrainment. The recovered gas can be quantified for a given case by taking the difference between the actual ventilation rate and the volume flow rate in the modeled interfacial shear layers. The flow rate in the shear layers is obtained using Eq. 11, and calibrated to a toroidal cavity for a given Fr_N and Re_N. To study this effect, consider a recovery factor defined as

$$C_Q = \left(1 - k_{RQ}\right) C_{Q,Spurk} \rightarrow k_{RQ} = 1 - \frac{C_Q}{C_{Q,Spurk}}. \qquad (14)$$

Note that Eq. 14 only remains valid for TSL cavities.

Physically, k_{RQ} is the fraction of gas entrained into the cavity-shear layer that is recovered back into the cavity. When k_{RQ} is between zero and one, a portion of the cavity-shear layer gas is recovered and returned to the cavity. Without accounting for this gas recovery, a straightforward application of the Spurk [1] model (Eq. 11) over predicts the gas entrainment rate for much of the curve, e.g. Fig. **11** (a). This is used as a measure of gas recovered back into the cavity via shear-layer thinning. Negative k_{RQ} values indicate that the total ventilation rate is higher than that entrained by the boundary layers, implying that an additional mechanism of entrainment is occurring. Presumably, in this condition, a favorable axial-pressure-gradient exists, corresponding to the PD-type cavity.

Recovery Factor in Hysteretic Cavities

The data collected in experiments conducted by Campbell and Hilborne [5] include hysteretic phenomena with twin-vortex and toroidal cavity closures. Their data is useful to develop models of the gas entrainment. The particular case examined uses a ventilated circular-disk cavitator at $Fr_N=16$ and $Re_N=62{,}000$. In Fig. **11** (a), a straightforward application of Eq. 11 (the unmodified model developed by Spurk [1] for non-buoyant cavities) is compared to the data of Campbell and Hilborne [5]. Eq. 11 yields an excellent prediction for the toroidal cavities, occurring on the right portion of the curve, through the increasing-C_Q hysteresis region. Beyond the hysteresis region, Eq. 11 clearly over predicts the ventilation rate (C_Q) required for a given cavity pressure (σ_c). For the time being, consider that the over prediction of the gas entrainment obtained using of Eq. 11 corresponds to the recovered gas; this is assessed in terms of k_{RQ}, and computed using Eq. 14. These quantities are plotted in Fig. **11** (b).

The trends in Fig. **11** (b), in the k_{RQ}-σ_c plot, display expected trends with an interesting behavior in the hysteretic (gray shaded) region. For toroidal cavities, k_{RQ} remains near zero, as expected. For twin-vortex cavities, k_{RQ} is bound between zero and one, suggesting that cavity shear layer recovery is occurring. In this region, an interesting feature is observed. For the twin-vortex regime (Q-decreasing curve), k_{RQ} is maximized at a near constant value of 0.64. This behavior implies that, in this region, the relative amount of gas recovered from the entrained-shear-layer gas remains constant and that the separated shear layer should be a dominant contributing mechanism to hysteresis. For the toroidal-vortex cavity, on the Q-increasing curve, k_{RQ} takes on a small negative value just prior to the cavity transition to a twin vortex. Perhaps, this is due to toroidal structures entraining additional cavity gas along with the shear-layer-entrained gas. Regardless, the consistency of the modeling with the data supports the concept of k_{RQ}.

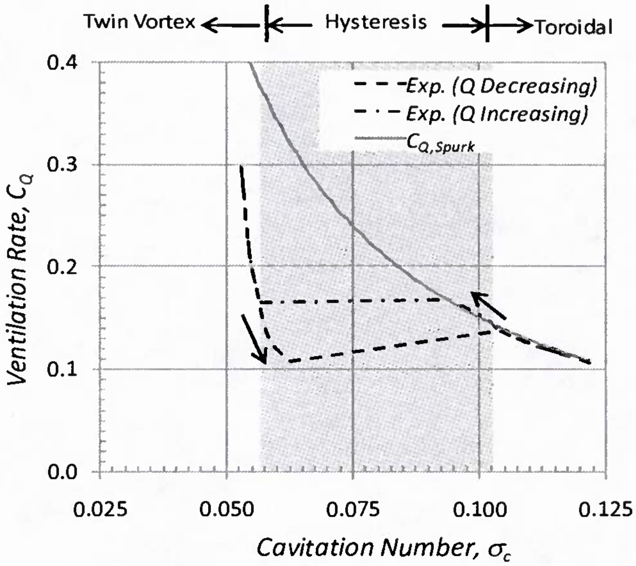

(a) C_Q-σ_c curves

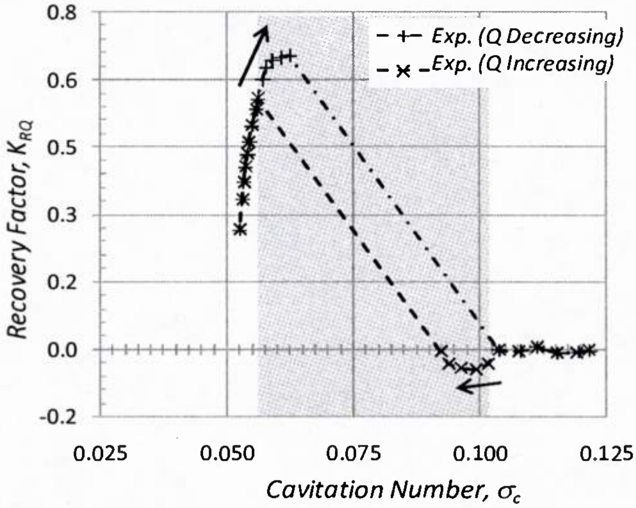

(b) Corresponding k_{RQ}, behavior

Figure 11: In part (a), is a comparison of a hysteretic C_Q-σ_c curve for a disk cavitator, from Campbell and Hilborne [5], to theory of Spurk [1]. Part (b) displays the corresponding k_{RQ} curves for the hysteretic cavity.

Approximating the Recovery Factor

Using physical arguments and experimental data, the recovery factor can be approximated. On the C_Q-σ_c space, there are essentially three regions that need to be considered, i.e. twin-vortex, hysteretic, and toroidal. Using Campbell and Hilborne's data [5], a path to approximate this behavior is proposed. First, we assess k_{RQ} as a function of σFr; this incorporates, the empirically determined [5], twin-vortex to toroidal-vortex transition criterion. Thus, a Heaviside function can be used to enforce this criterion in the k_{RQ} approximation for σFr values greater than unity, i.e. $H(1-\sigma Fr)$. For the twin-vortex range, outside of the hysteresis region, a polynomial function with a minimum at $\sigma Fr=1$, $k_{RQ}=1$ fits the data. Finally, it was observed above that within the hysteretic region of the twin-vortex cavities, k_{RQ} is maintained at a constant value, $k_{RQ,Hys}$. This and a minimal value of zero are used to bound the function. The approximation is given as

$$k_{RQ}(\sigma Fr)=\max\left(\min\left(A_0+A_2(\sigma Fr-1)^2,k_{RQ,Hys}\right),0\right)H(1-\sigma Fr), \qquad (15)$$

where the values of A_0 and A_2 were determined via a least squares fit to the data. For this specific case (from the experiments of Campbell and Hilborne [5]), A_0=0.815, A_2=-17.36, $k_{RQ,Hys}$=0.654, and the Heaviside function is approximated as $H(1-\sigma Fr) \approx 0.5[1+\tanh(1000\{1-\sigma Fr\})]$. The approximations are plotted below in Fig. **12** and follow the data quite well.

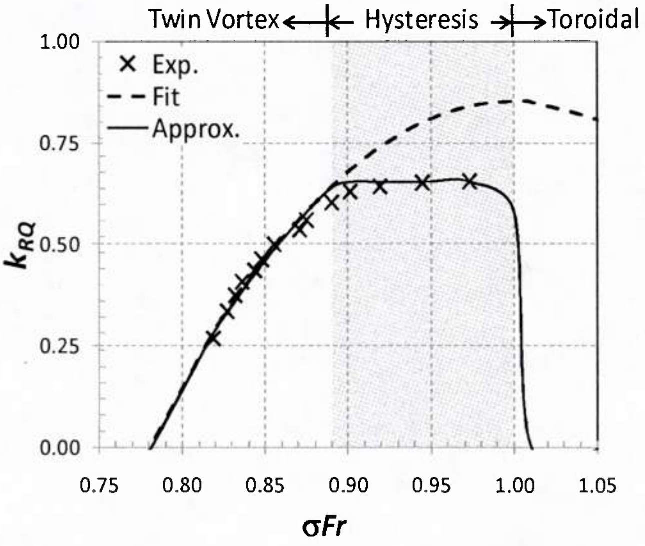

Figure 12: Recovery factor versus σFr for the experiment and approximate function.

The model appears to conform well to this particular case. The amount of shear layer entrained gas, $C_{Q,SL}$, from Eq. 14 using the empirical correction to the recovery factor, k_{RQ}, is compared to experimental measurements in Fig. 13. It is apparent that the model predicts the experimental data well. However, it appears that, approaching the highest C_Q and lowest σ_c values, the model remerges into the $C_{Q,Spurk}$ curve, a undesired feature based on the mechanisms previously described.

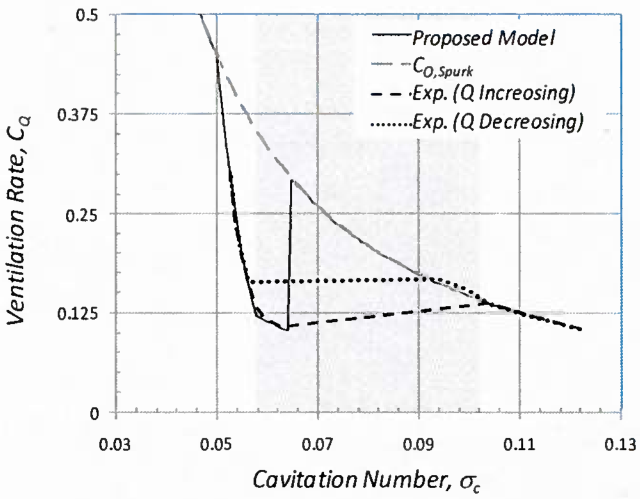

Figure 13: Predicted gas entrainment rates using the proposed model with shear recovery, Spurk's model ($C_{Q,Spurk}$), and experiments from Campbell and Hilborne [5].

Although the presented approximation is an empirical fit to the data, a model of the physics is preferred. Such a model could enable an analytic function that remains valid over a range of conditions. It is presumed that this approximation is valid only for this particular Re_N and Fr_N. However, with additional data the parameters A_0, A_2, and $k_{RQ,Hys}$ could be empirically determined using extended Re_N and Fr_N data sets. Such an approach should enable valid approximations over various cavitator configurations and conditions.

Shear-Layer Gas and Potential Relation to Hysteresis

Consider various model behaviors with respect to experimental measurements in Fig. 14. The $C_{Q,CHm}$ (Eq. 10) prediction, with an assumed vortex velocity, $V_{VT}=V_\infty$ is compared to $C_{Q,Spurk}$ (Eq. 11) prediction, and hysteretic experimental data [5]. The $C_{Q,CHm}$ curve underpredicts C_Q for toroidal cavities, overpredicts C_Q for twin-vortex cavities near hysteresis, and that if the experimental data were extrapolated to higher ventilation rates, it would merge into the $C_{Q,CHm}$ prediction. Suggesting that the $C_{Q,CHm}$ prediction is most valid at high ventilation rates. Whereas the $C_{Q,Spurk}$-curve only matches the toroidal-vortex region. Thus, a combination of these two models present a path to modeling the correct behavior.

Comparing the $C_{Q,CHm}$- and $C_{Q,Spurk}$-σ curves reveals interesting behavior relating to hysteresis. These curves intersect near the lowest point in the twin-vortex cavity hysteresis region, implying that the physics represented by the two models can be related to the hysteresis phenomenon. In terms of the modeled physics, this intersection occurs when the twin vortex tubes are just sufficiently large enough to support the shear-layer gas. This could potentially be used as an indicator of the transition from twin-vortex back to toroidal cavity closure. Another interpretation is that the cavity remains in a twin-vortex state provided that the vortex tubes can support the volume of entrained gas within the cavity attached shear layers. However, this area is based on a effective "displacement thickness" rather than a "shear-layer thickness" (similar to a boundary layer thickness), suggesting that the vortex cores not need be adequate to support the entire shear layer, but perhaps just the high-velocity, most tightly entrained, portions. Then, the more slowly moving, but still attached, portion of the shear layer would be the gas susceptible to recovery. This appealing concept and fits the present data nicely, but requires additional support in data and/or observations.

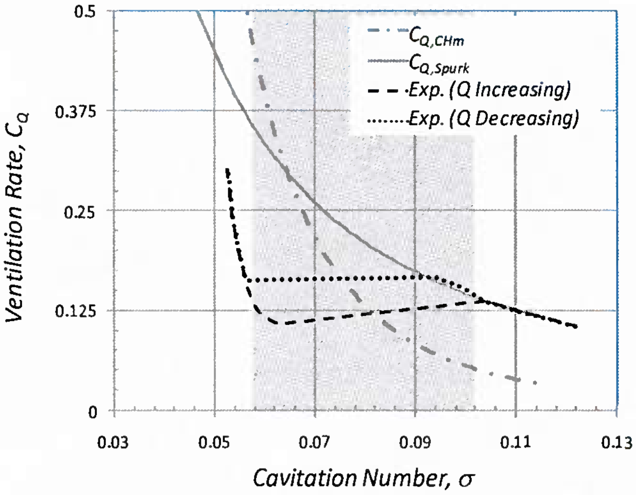

Figure 14: Predicted gas entrainment rates using Campbell and Hilborne's model ($C_{Q,CHm}$), Spurk's model ($C_{Q,Spurk}$), and experiments from Campbell and Hilborne [5].

Pressure Driven Gas Entrainment

Referring to the form of the present model (Eq. 13), a model is still lacking the pressure-gradient driven gas entrainment processes, or $C_{Q,p}$. Recall from Fig. 14, that the modified Campbell and Hilborne [5] model, $C_{Q,CHm}$, displays the expected trend at high C_Q values, thus, the model and assumption that $V_{VT}=V_\infty$ will be utilized. Therefore, an initial guess of $C_{Q,p}$ will be given by the difference between $C_{Q,CHm}$ and $C_{Q,Spurk}$. However, to obtain a smooth transition, from the model TSL cavity to the model PD cavity, this quantity is multiplied by $(1-k_{RQ}/\,k_{RQ,Hys})^2$. The resulting model is then

$$C_{Q,p} = \max\left(C_{Q,CHm} - C_{Q,Spurk}, 0\right)\left(1 - \frac{k_{RQ}}{k_{RQ,Hys}}\right)^2 . \qquad (16)$$

The combined results of Eqns. 14 and 16, substituted into the proposed model (Eq. 13), are plotted in Fig. 15. Note that the prediction conforms nicely to the data for toroidal and twin vortex cavities, and behaves as expected approaching high C_Q values.

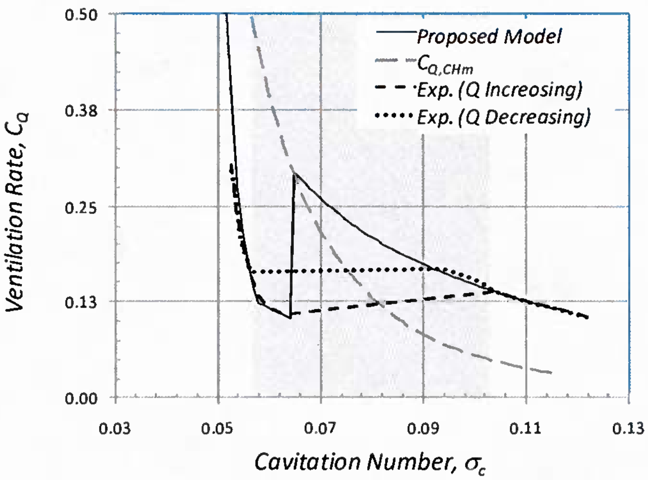

Figure 15: Gas entrainment rates using the proposed model, Campbell & Hilborne model ($C_{Q,CHm}$), and experiments from Campbell and Hilborne [5].

Application of Model

Finally, to verify that it continues to produce valid results beyond the initial case the model is applied over a broad range of Froude numbers. As shown in Fig. **16**, using the 1 inch diameter cavitator data from the experiments of Campbell and Hilborne [5], the model produces reasonable gas-entrainment-rate predictions over a range of conditions. In these cases, the empirical parameters (A_0, A_2, and $k_{RQ,Hys}$) are established using a least-squares fit to the data. As no toroidal closure data is available, the constant k_Q is determined using the observation from Fig. 14, that $C_{Q,CHm}$ and $C_{Q,Spurk}$ intersect at the minimum C_Q that can sustain a twin-vortex cavity. This method of specifying k_Q is only a single observation. Additional hysteretic data is needed for further assessment. In any case, a reasonable extrapolation from data in the twin-vortex range into the toroidal regime is presented.

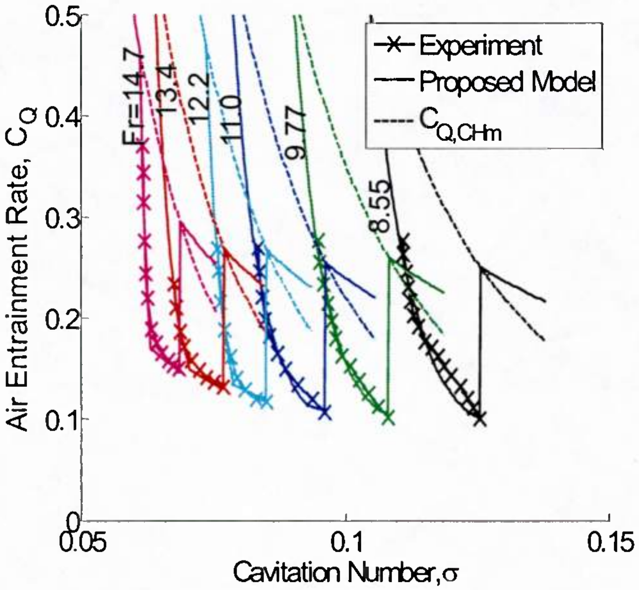

Figure 16: Gas entrainment rates using the proposed model and experiments from Campbell and Hilborne [5].

Summary of the Present Model

Here we summarize the new model formulation. From Eq. 13 we define the gas entrainment rate as the combination of shear-layer gas and gas exiting through pressure-gradient mechanisms as

$$C_Q = C_{Q,SL} + C_{Q,p}.$$

The shear-layer component is defined through a modified form of the model of Spurk, accounting for recovered gas from the shear layers, given in Eq. 14 as

$$C_{Q,SL} = \left(1 - k_{RQ}\right) C_{Q,Spurk} \ \&$$

$$C_{Q,Spurk} = k_Q \frac{(1+\sigma)}{\sigma} \sqrt{\frac{1}{\sigma} \ln \frac{1}{\sigma}}.$$

Note that recovery factor is presently an empirically determined term, estimated using Eq. 15,

$$k_{RQ}\left(\sigma Fr\right) = \max\left(\min\left(A_0 + A_2\left(\sigma Fr - 1\right)^2, k_{RQ,Hys}\right), 0\right) H\left(1 - \sigma Fr\right).$$

Finally, the pressure-gradient entrainment processes are modeled using previous theory of the vortex-tube size as a basis; the model is represented in Eq. 16, or

$$C_{Q,p} = \max\left(C_{Q,CHm} - C_{Q,Spurk}, 0\right)\left(1 - \frac{k_{RQ}}{k_{RQ,Hys}}\right)^2$$

$$C_{Q,CHm} = \frac{\pi A^2 \left(1+\sigma\right)^2}{47.6 k Fr_{N,Disk}^4 \sigma^4}$$

These terms form the proposed model, which relies on three additional empirical constants, A_0, A_2, $k_{RQ,Hys}$.

CONCLUSIONS

Using viscous-based CFD simulations of long and slender cavities generated behind an axisymmetric cavitator, the gaseous flow regions within the cavity has been analyzed. For such cavities, the essence of the cavity-gas entrainment processes is observed to relate to the cavity-interface-attached shear layer, an observation that corroborates the theory of Spurk [1]. These observations indicate that the shear layer mechanism also contributes to the gas entrainment from twin-vortex cavities. The importance of these shear layers was shown related to CFD-based numerical schemes for supercaviting flows, models of gas entrainment, and an improved understanding of gaseous flow regions in a supercavity.

The behavior of the entrainment process was repeatable and present in numerous modeled cavities. The process initiates rather abruptly, as the ventilation gas is entrained directly to the shear layer just aft of the cavitator. Moving downstream of the cavitator, the shear layer thickens, until, approximately, the maximum radius of the cavity, where it was observed that a shear-layer thinning mechanism initiates. Adverse pressure gradients, typical at the aft end of the cavity, are a likely mechanism that drives this thinning shear layer. At the cavity-closure region, the amount of gas actually departing the cavity is finally determined. If the closure mechanism is toroidal vortex, the shear layer entrained gas at the closure will exit unabated. If the closure mechanism is twin vortex, portions of the shear-layer entrained gas are likely to be stripped off and recovered back into the cavity.

These observations have been used to formulate improved models of gas entrainment, address issues with CFD turbulence modeling approaches, and highlight potential experimental scaling issues. When applied straightforwardly, RANS approaches tend to overpredict the amount of gas entrained within cavity shear layers, ultimately over predicting C_Q. Approaches that reduce the modled eddy viscosity within these shear layers, thus, are sensible. Additionally, Reynolds number effects on the internal cavity gas flow also show potential importance, in particular when considering body-filled cavities. Although integral effects may be small, such as cavity size and/or pressure, the internal flow effect is significant, which may be an overlooked scaling issue. Lastly, an improved gas-entrainment model is proposed, combining the models of Campbell and Hilborne [5] with that of Spurk [1], and includes an additional model of shear-layer gas recovery. The final model displays an ability to capture hysteresis over a wide range of Froude numbers.

ACKNOWLEDGMENTS

This work was supported by the Office of Naval Research, under contract #N00014-07-1-0134, with Dr. Kam Ng as the program manager and contract #N00014-09-10042, with Dr. Ronald Joslin as the program manager. Furthermore, much gratitude is given to Dr. Mark Maughmer, Dr. Phillip Morris, and Dr. Ralph Noack of The Pennsylvania State University and Dr. David Hill of Oregon State University for their comments and insights added with respect to this work.

NOMENCLATURE

Symbols

C_L	three-dimensional lift coefficient, $L/(\rho_\infty V_\infty^2 D_N^2 \pi/4)$
C_D	three-dimensional drag coefficient, $D/(\rho_\infty V_\infty^2 D_N^2 \pi/4)$
C_Q	ventilation rate coefficient, $QV_\infty^{-1}D^{-2}$
$C_{Q,l}$	local gas entrainment rate, $\alpha u/V_\infty$
$C_{Q,CHm}$	modified Campbell and Hilborne model of C_Q
$C_{Q,Spurk}$	modified Spurk model of C_Q
$C_{Q,p}$	pressure-gradient driven C_Q terms
$C_{Q,SL}$	shear-layer driven C_Q terms
D_N	cavitator diameter
g	gravity
H	heavyside function
k_Q	empirical constant for shear-layer entrainment rate
k_{RQ}	portion of recovered shear-layer gas
L_c	cavity length
Q	ventilation rate
R_c	cavity radius
R_N	cavitator radius
Re	Reynolds number, $\rho VL/\mu$

V	velocity
V_I	Integrated cavity volume
V_{VT}	axial velocity in vortex tube

Greek Symbols

α	gas volume fraction
μ	molecular viscosity
ν	dynamic viscosity
ρ	density
σ_c	cavitation number based on cavity pressure, $(p_\infty - p_c)/q_\infty$

Subscripts

c	reference to cavity properties
$Disk$	reference shape to an effective disk
l	reference to local properties
N	reference to cavitator diameter
∞	reference to free stream

REFERENCES

[1] Spurk, J.H. "On the Gas Loss from Ventilated Supercavities," *Acta Mechanica*, vol. 155, pp. 125-135, 2002.

[2] May, A., "Water Entry and the Cavity-Running Behavior of Missiles," Naval Sea Systems Command Hydroballistics Advisory Committee Technical Report 75-2, 1975.

[3] Semenenko, V.N., "Artificial Supercavitation. Physics and Calculation," VKI Lecture Series on Supercavitating Flows, VKI Press, Brussels, Feb. 2001.

[4] Logvinovich, G.V., *Hydrodynamics of Free-Boundary Flows*, Israel Program for Scientific Translation, 1969.

[5] Campbell, I.J., Hilborne, D.V., "Gas Entrainment Behind Artificially Inflated Cavities," 2nd Symposium on Naval Hydrodynamics, Washington D.C., USA, 1958.

[6] Epshtein, L.A., "Characteristics of Ventilated Cavities and Some Scale Effects," Unsteady Water Flow with High Velocities, Proceedings of IUTAM Symposium, Leningrad, USSR, 1971. Reprinted with translation from NAUKA Publishing House, Moscow, 1973.

[7] Lindau, J.W., Kunz, R.F., Boger, D.A., Stinebring, D.R., and H.J. Gibeling, "High Reynolds number, unsteady, multiphase CFD modeling of cavitating flows," *Journal of Fluids Engineering*, Transactions of ASME, vol. 124(3) pp. 607-616, 2002.

[8] Kinzel, M. P. Computational Techniques and Analysis of Cavitating-Fluid Flows. Dissertation in Aerospace Engineering, University Park, PA, USA : The Pennsylvania State University, May 2008.

[9] Kiceniuk, T., "An Experimental Study of the Hydrodynamic Forces Acting on a Family of Cavity Producing Conical Bodies of Revolution," California Institute of Technology-Hydrodynamics lab, Report E-12-17, June 1954.

[10] Wosnik, M., Schauer, T.J., and Arndt R.E.A., "Experimental Study of a Ventilated Supercavitating Vehicle," Fifth International Symposium on Cavitation (CAV2003), Osaka, Japan, November 1-4, 2003.

[11] Schauer, T.J., "An Experimental Study of a Ventilated Supercavitating Vehicle, MS Thesis, Department of Aerospace Engineering and Mechanics, University of Minnesota, 2003.

[12] Kinzel, M.P., Lindau, J.W., Peltier, L.J., Zajaczkowski, F., Arndt, R.A., Wosnik, M., Mallison, T., "Computational Investigations of Gas Entrainment, Hysteresis, and Loading for Large-Scale, Buoyant Cavities," 9th International Conference on Numerical Ship Hydrodynamics, Ann Arbor, Michigan, August 5-8, 2007.

[13] Kinzel, M.P., Lindau, J.W., Peltier, L.J., Kunz, R.F, and Sankaran, V., "Detached-Eddy Simulations for Cavitating Flows," AIAA Paper No. 2007-4098, 18th AIAA Computational Fluid Dynamics Conference, Miami, FL, USA, June, 2007.

[14] Cox, R.N., Clayden, W.A., "Gas Entraiment at the Rear of a Steady Cavity," Cavitation in Hydrodynamics, London, 1956.

[15] Benjamin, T.B., "Effects of a Flexible Boundary on Hydrodynamic Stability," *Journal of Fluid Mechanics*, Vol. 9, p4, pp. 513-532, 1960.